Liquid Crystals
Publication details, including instructions for authors and subscription information:
http://www.informaworld.com/smpp/title~content=t713926090

Texture dependence of capillary instabilities in nematic liquid crystalline fibres

Ae-Gyeong Cheong[a]; Alejandro D. Rey Corresponding author[a]
[a] Department of Chemical Engineering, McGill University, Montreal, Quebec, Canada H3A 2B2

Online publication date: 21 May 2010

To cite this Article Cheong, Ae-Gyeong and Rey Corresponding author, Alejandro D.(2004) 'Texture dependence of capillary instabilities in nematic liquid crystalline fibres', Liquid Crystals, 31: 9, 1271 — 1284
To link to this Article: DOI: 10.1080/02678290412331282109
URL: http://dx.doi.org/10.1080/02678290412331282109

LIQUID CRYSTALS, VOL. 31, NO. 9, SEPTEMBER 2004, 1271–1284

Texture dependence of capillary instabilities in nematic liquid crystalline fibres

AE-GYEONG CHEONG and ALEJANDRO D. REY*

Department of Chemical Engineering, McGill University, 3610 University Street, Montreal, Quebec, Canada H3A 2B2

(*Received 26 September 2003; in final form 18 May 2004; accepted 25 May 2004*)

Static and dynamic linear analyses of axisymmetric capillary instabilities in textured nematic liquid crystalline fibres are performed using the equations of nemato-statics and inviscid nemato-dynamics. Three representative textures, viz. axial, onion, and radial, are analysed to show all possible effects of Frank gradient elasticity on the wavelength selection and growth rate of peristaltic modes driven by surface area reduction. It is found that Frank elasticity may tend to stabilize or destabilize the fibre, depending on the initial fibre texture. Axial textures tend to stabilize the fibre through the director splay–bend distortions driven by surface tilting. Onion textures are destabilized by decreasing azimuthal bend elastic energy caused by surface displacement. Radial textures exhibit a stabilizing tilt mechanism due to bend modes and a destabilizing displacement mechanism due to splay modes, but the former is predicted to be dominant. The static analysis provides good estimates of the instability thresholds while the transient energy balance provides information on the fastest growing modes. The static and dynamic results are compared and shown to be fully consistent. The couplings between splay and/or bend distortions, surface tilting, and surface displacement in nematic fibres are characterized and used to explain the deviations from the classical Rayleigh instability.

1. Introduction

The current wide use of thin fibres, films and multiphase material systems demands a fundamental understanding of capillary hydrodynamics, interfacial thermodynamics, and interfacial transport phenomena [1–3]. Many new liquid crystal applications involving dominant interfacial effects such as mesophase fibre spinning [4] and formation of *in situ* liquid crystal polymer composites [5] likewise require a fundamental understanding of capillary hydrodynamics. Although interfacial liquid crystal thermodynamics is a highly developed field [6–14], non-equilibrium surface phenomena are not well understood and/or characterized. Force balance equations describing static [15–20] and dynamical interfacial phenomena [17, 20] are available but have not been widely used in describing the mechanics of fibre and film microstructures. This paper is concerned with the stability of a nematic liquid crystalline fibre.

A question of fundamental importance in capillary instabilities of liquid crystalline fibres is to identify possible mechanisms that promote stability and hence widen the processing windows for these materials. In isotropic fluid fibres, the surface tension driven fiber-to-droplet transformation is well understood and known as the Rayleigh instability [1, 2, 21]. In the static thermodynamical analysis, the Rayleigh threshold shows that the isotropic fibre is unstable for the wavelength of the surface disturbance exceeding the perimeter of the fibre. Meanwhile, Rayleigh also predicted a fastest growing wavelength that governs the capillary instability of an isotropic fluid fibre and thus makes the fibre break up into a trail of droplets with a specific size in the linear regime using a transient analysis. For isotropic fluid fibres, only surface area reduction plays a role to promote instability since the surface energy decreases by decreasing the surface area [5]. On the other hand, an essential characteristic of nematic liquid crystals is mechanical anisotropy and bulk gradient elasticity [22]. Bulk gradient elasticity (also known as Frank elasticity) in nematic liquid crystals is due to orientation gradients and hence is known as curvature elasticity. The anisotropies in the viscoelastic bulk properties of nematic liquid crystals are well understood theoretically [23, 24] and experimentally [22], and the anisotropies in the surface elastic properties of nematics are also well characterized [7, 9]. Capillary instabilities in liquid crystalline fibres have

*Author for correspondence; e-mail: alejandro.rey@mcgill.ca

Liquid Crystals ISSN 0267-8292 print/ISSN 1366-5855 online © 2004 Taylor & Francis Ltd
http://www.tandf.co.uk/journals
DOI: 10.1080/02678290412331282109

been analysed with surface anisotropies [25–27], and in this paper we analyse the bulk anisotropy effects on the instability mechanisms and thresholds. For clarification, we note that anisotropy in this paper refers to the unique direction imposed by the average molecular orientation, known as the nematic director, and hence different director fields correspond to different types of anisotropy. Thermodynamic stability analyses of nematic LC fibres have been performed for different nematic textures [5, 28]. In this paper we extend the previous work by considering the time evolution of unstable modes in axial, onion, and radial textures, as well as by establishing the correspondence between instability criteria found using thermodynamical and dynamical analyses. The fibre is assumed to have nematic orientation, where the rod-like molecules are more or less parallel to each other but otherwise free to translate past each other [22]. As mentioned above the theories and analyses are based on transient integral energy balances as well as free-energy calculations so that we capture growth rate patterns of instabilities as well as static instability thresholds.

The specific objectives of this paper are to: (1) formulate a thermodynamic model for the static analysis and present an integral energy balance equation for the transient analysis that describes and identifies the bulk elastic energy contributions to capillary instabilities of nematic liquid crystalline fibres; (2) derive instability criteria for static and transient analyses in three characteristic nematic textures and elucidate the physical mechanisms that promote and suppress the instabilities; (3) establish parametric conditions that lead to capillary instabilities; (4) characterize the nematic orientation contributions to capillary instabilities; (5) relate the Frank distortion energy contribution in the static analysis to that in the transient analysis.

The organization of this paper is as follows. In § 2, we present the thermodynamic model for static analysis, the integral energy balance equation for transient analysis, and the equilibrium condition for distorted director fields. In § 3, we derive the instability criteria for static and transient energy analyses in three characteristic nematic textures. The instability mechanisms for static and transient analyses are clearly identified and discussed in terms of Frank distortion elastic energy. § 4 presents conclusions.

2. Governing equations

2.1. *Geometry and texture of nematic liquid crystalline fibres*

To define the state of a nematic liquid crystalline fibre completely, both the geometry of the fibre and the spatial orientational order of the nematic liquid crystal must be specified. More specifically we define: Nematic Liquid Crystalline Fibre $\equiv \{\mathbf{n}, R, \mathbf{N}\}$, where $\mathbf{n}$ is the nematic director field [22], R is the fibre radius, and $\mathbf{N}$ is the unit surface normal vector. For an isotropic material fibre, only the geometry is necessary, i.e. $\{R, \mathbf{N}\}$.

Figure 1 shows definitions of the fibre geometry. Figure 1 (*a*) shows that the fibre is initially a uniform cylinder with radius a, with its axis collinear with the z-axis of a cylindrical coordinate system. In the cross-sectional view, unit vectors $\mathbf{i}_r$ and $\mathbf{i}_\theta$ are shown in the direction of the r- and θ-axes, respectively. Figure 1 (*b*) shows the periodically deformed fibre with unit surface normal $\mathbf{N}$, radius R and wavelength λ. The fiber radius R and unit surface normal $\mathbf{N}$ periodically change with a wavelength λ along the z-direction. In this paper, we apply our analysis to three characteristic nematic textures of initially constant director fields, denoted as axial, onion, and radial textures, and accordingly the nematic fibre with each texture is called axial fibre, onion fibre, and radial fibre, respectively. Figure 2 shows the schematic of undeformed fibres with (*a*) axial, (*b*) onion and (*c*) radial textures. In the cross-sectional view, the director field $\mathbf{n}$ is shown as dots, curves, or lines in each texture. The fibre nematic texture is expressed by the director field using unit vectors $\mathbf{i}_z$, $\mathbf{i}_\theta$ and $\mathbf{i}_r$ in the direction of the z-, θ- and r-axes, respectively. Defect cores are seen at the centre of onion and radial textures. In this paper, we assume that these defects have already nucleated.

It is noted that escaped radial textures in cylindrical cavities are well understood experimentally and

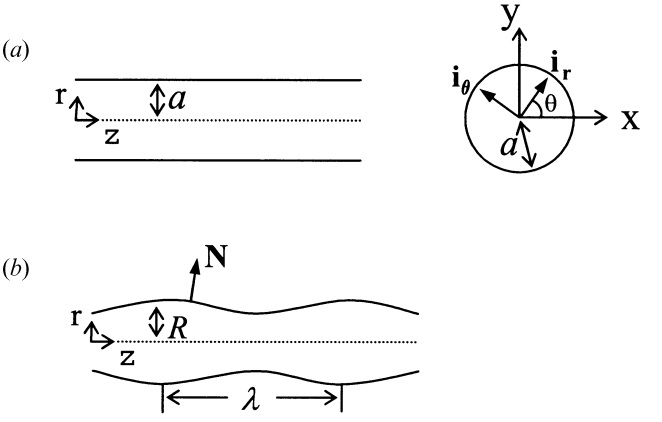

Figure 1. (*a*) Unperturbed fibre with radius a is aligned in the z-axis of a cylindrical coordinate system (r, θ, z). Cross-sectional view in Cartesian coordinates (x, y) shows the unit vectors $\mathbf{i}_r$ and $\mathbf{i}_\theta$ and azimuthal angle θ. (*b*) Periodically deformed axisymmetric fibre with unit surface normal vector $\mathbf{N}$, radius R and wavelength λ. Fibre radius R and unit surface normal $\mathbf{N}$ periodically change with wavelength λ along the z-direction. The figure is representative of the peristaltic mode.

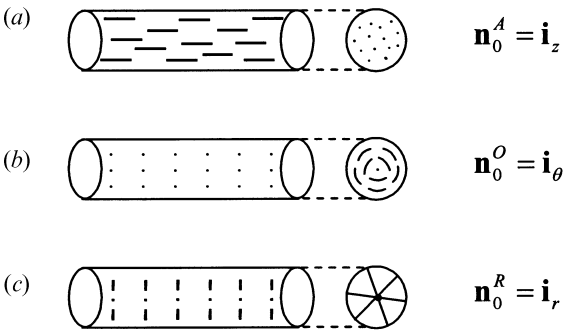

Figure 2. Schematic of undeformed fibres with (*a*) axial, (*b*) onion and (*c*) radial textures. In the cross-sectional view, the director field **n** is shown as dots, curves or lines in each texture. Defect cores are seen at the centre of onion and radial textures. The corresponding director field is shown on the right of the figures.

theoretically. The escaped radial texture where the director escapes into the third dimension along the cylinder axis has been shown to be more stable than the radial texture with a line defect at the centre [22, 29, 30], and was observed for MBBA in cylindrical cavities [30, 31]. The escaped radial textures with singular point defects along the cylinder axis were also observed in cylindrical cavities of $20 \sim 200\,\mu m$ in radius by optical studies [31, 32] and of as small as $0.3\,\mu m$ in radius by deuteron NMR, where the density of singular point defects was obtained in the strong anchoring limit [33]. Meanwhile, the radial texture with a line defect at the centre of the fibre can also be stable, for instance, in the vicinity of a nematic/smectic A transition [22] or when the fibre radius is small enough [22, 29, 30].

Linear stability analysis is used to describe peristaltic axisymmetric capillary instabilities in nematic liquid crystalline fibres for the three textures. Static energy analysis based on thermodynamic stability is presented to obtain a critical wavelength for the capillary instability while transient energy analysis is used to construct a growth rate curve and thus obtain the fastest growing wavelength as well as to establish the consistency of the results. Twist distortions are beyond the scope of this paper, and only splay and/or bend modes are taken into account. Likewise, chiral non-axisymmetric distortion modes are not taken into account in this paper.

2.2. *Static energy analysis*

We consider the thermodynamic stability of an infinitely long cylindrical nematic LC fibre subjected to infinitesimal periodic surface disturbances. The nematic liquid crystal is assumed to be incompressible, and its initial orientation is homogeneous in each of three characteristic textures: axial, onion and radial. Then, the director fields evolve as the shape of nematic fibres changes.

As seen in figure 1 (*b*), the fiber radius R and the unit surface normal **N** change along the z-direction. In the static analysis, the fibre shape with a periodic surface disturbance is given at any position z by

$$R(z) = R_0 + \xi(z). \tag{1}$$

The periodic surface disturbance ξ is expressed as

$$\xi(z) = \xi_0 \cos[kz] \tag{2}$$

where ξ_0 is the initial amplitude of the disturbance and k the axial wavenumber. The average fibre radius R_0 in equation (1) is required, for a fixed volume, to be

$$R_0 = a\left(1 - \frac{\xi_0^2}{2a^2}\right)^{\frac{1}{2}} \approx a\left(1 - \frac{\xi_0^2}{4a^2}\right) \tag{3}$$

where the approximation is valid in the linear regime of the capillary instability, i.e. when

$$\frac{\xi}{a} \ll 1. \tag{4}$$

The unit surface normal **N** is given in the linear regime by

$$\mathbf{N} = \mathbf{i}_r - \frac{\partial R}{\partial z}\mathbf{i}_z. \tag{5}$$

During the capillary instability, the fibre geometry evolution is captured by the principal radii of curvature ($R_{r\theta}$, R_{rz}) as well as the fibre radius R and its unit surface normal **N**. In the linear regime, the principal radii of the curvature are expressed as [21]

$$\frac{1}{R_{r\theta}} = \frac{1}{R}; \quad \frac{1}{R_{rz}} = -\frac{\partial^2 R}{\partial z^2}. \tag{6}$$

To discuss capillary instabilities, it is also useful to introduce the following expression for the mean curvature H in cylindrical coordinates:

$$H = -\frac{1}{2}\nabla_s \cdot \mathbf{N} = -\frac{1}{2}\left(\frac{1}{R_{r\theta}} + \frac{1}{R_{rz}}\right) \tag{7}$$

$$= -\frac{1}{2}\left(\frac{1}{R} - \frac{\partial^2 R}{\partial z^2}\right) \tag{8}$$

where ∇_s is the surface gradient operator.

2.2.1. *Distorted director fields*

As seen in figure 2 (*a*), in the axial texture, the director is initially oriented along the fibre axis and it is given by

$$\mathbf{n}_0^A = \mathbf{i}_z \tag{9}$$

where the superscript A denotes the axial texture and the subscript 0 the initial director field. Likewise, in figure 2 (*b*), the director is initially along the azimuthal

direction in the onion texture:

$$\mathbf{n}_0^O = \mathbf{i}_\theta \tag{10}$$

and, in figure 2(*c*), along the fibre radius in the radial texture:

$$\mathbf{n}_0^R = \mathbf{i}_r \tag{11}$$

where the superscripts O and R denote the onion and radial textures, respectively. The director field in each texture is expected to evolve as the nematic fibres are subjected to infinitesimal surface disturbances. Since the surface disturbances are very small, only a slight distortion from the initial director field is assumed [22]:

$$\mathbf{n} = \mathbf{n}_0 + \epsilon \tag{12}$$

where $\mathbf{n}_0$ is the initial director field and ϵ is the slight distortion normal to $\mathbf{n}_0$.

To find the distorted director field in each texture, we apply conditions for equilibrium in the nematic bulk by introducing the distortion free energy. The distortion free energy density, known as Frank distortion energy, stored in a nematic LC fibre is simplified using one constant approximation to [22]

$$F_\mathrm{d} = \frac{K}{2}\left[(\nabla\cdot\mathbf{n})^2 + (\nabla\times\mathbf{n})^2\right] \tag{13}$$

where F_d is the Frank distortion free energy density and K the Frank elastic constant in the one constant approximation. In equilibrium, the following condition is satisfied:

$$\mathbf{n}\times\mathbf{h} = 0 \tag{14}$$

where $\mathbf{h}$ is the molecular field expressed as [22]

$$\begin{aligned}\mathbf{h} &= -\left[\frac{\partial F_d}{\partial \mathbf{n}} - \nabla\cdot\frac{\partial F_d}{\partial(\nabla\mathbf{n})}\right] \\ &= K\nabla^2\mathbf{n}.\end{aligned} \tag{15}$$

Equation (14) means that the director is parallel to the molecular field in equilibrium.

2.2.2. *Free energy of nematic liquid crystalline fibres*

The total free energy density for a nematic LC fibre with distorted director orientation is given by [22]:

$$F = F_\mathrm{d} + F_\mathrm{s} = \frac{K}{2}\left[(\nabla\cdot\mathbf{n})^2 + (\nabla\times\mathbf{n})^2\right] + \gamma\delta(r-R) \tag{16}$$

where F_s is the surface free energy density for the surface director orientation along the easy axis, γ the surface free energy density, and δ the Dirac delta function. Since the strong anchoring condition is assumed at the fibre surface, the surface free energy density γ only represents the isotropic surface tension. Thus, the surface free energy contribution to the total free energy contains no elastic distortion effect and remains unchanged in the three nematic textures. Meanwhile, the Frank distortion energy contribution differs in one texture from another since the director variation in the bulk of the fibre is the origin of the elastic distortion energy.

2.3. *Transient energy analysis*

We consider the transient stability of an infinitely long cylindrical nematic LC fibre subjected to infinitesimal periodic surface disturbances. The geometries of the LC fibre and the director field are a function of time as well as of space. In this section, the general equation of the transient integral energy balance is derived.

In the transient analysis, the fibre shape at any time t and position z is given by

$$R(z,t) = R_0 + \xi(z,t). \tag{17}$$

The surface disturbance ξ is expressed by assuming its exponential growth as

$$\xi(z,t) = \xi_0\cos[kz]\exp(\alpha t) \tag{18}$$

where α is the growth rate for real and positive values.

2.3.1. *Transient integral energy balance equation*

The conservation of energy under isothermal condition, and under the absence of body forces, director inertia and director surface force is given by [10]:

$$\frac{\mathrm{d}}{\mathrm{d}t}\int_V\left(\frac{1}{2}\rho v\cdot v + F_\mathrm{d}\right)\mathrm{d}V + \int_V T\dot{S}\,\mathrm{d}V = \int_A \mathbf{N}\cdot\mathbf{t}\cdot v\,\mathrm{d}A \tag{19}$$

where $\frac{\mathrm{d}}{\mathrm{d}t}$ and the superposed dot denote material time derivatives, ρ is the density, v the velocity, T the temperature, S the entropy per unit volume, $\mathbf{t}$ the stress tensor, V the volume, and A the surface area. If the only entropy source is the viscous dissipation, the second integral in equation (19) becomes [22]

$$\int_V T\dot{S}\,\mathrm{d}V = \int_V \mathbf{A} : \mathbf{t}^v\,\mathrm{d}V. \tag{20}$$

The rate of deformation tensor $\mathbf{A}$ is expressed as

$$\mathbf{A} = \frac{1}{2}\left[(\nabla v) + (\nabla v)^\mathrm{T}\right] \tag{21}$$

where the superscript T denotes the transpose. The viscous stress tensor $\mathbf{t}^v$ is given as

$$\mathbf{t}^v = 2\mu\mathbf{A} \tag{22}$$

where μ is the viscosity. It is noted that in the linear regime distortions are insignificant and the rheology is Newtonian [22]. By making use of equations (21) and (22) in (20), equation (19) can be rewritten in the linear

regime such that

$$\int_V \left[\frac{\partial}{\partial t}\left(\frac{1}{2}\rho v\cdot v\right)+\dot{F}_{\mathrm{d}}\right]\mathrm{d}V + \int_V \frac{1}{2}\mu\left[(\nabla v)+(\nabla v)^{\mathrm{T}}\right]:\left[(\nabla v)+(\nabla v)^{\mathrm{T}}\right]\mathrm{d}V = \int_A \mathbf{N}\cdot\mathbf{t}\cdot v\,\mathrm{d}A. \quad (23)$$

Because strong anchoring condition is imposed at the fibre surface, the surface behaves like an isotropic material and only the contribution of $\dot{F}_{\mathrm{d}}$ reflects the anisotropic elasticity of the LC fibre. Using equation (13), the contribution of $\dot{F}_{\mathrm{d}}$ in (23) is expressed in terms of $\nabla\mathbf{n}$:

$$\dot{F}_{\mathrm{d}}=\frac{\partial F_{\mathrm{d}}}{\partial(\nabla\mathbf{n})}:\frac{\mathrm{d}}{\mathrm{d}t}(\nabla\mathbf{n})^{\mathrm{T}}=K\left[(\nabla\cdot\mathbf{n})(\mathrm{tr}\mathbf{D})+\nabla\mathbf{n}:\mathbf{D}-\nabla\mathbf{n}:\mathbf{D}^{\mathrm{T}}\right] \quad (24)$$

where $tr\mathbf{D}$ denotes the trace of tensor $\mathbf{D}$ and

$$\mathbf{D}\equiv\frac{\mathrm{d}}{\mathrm{d}t}(\nabla\mathbf{n})^{\mathrm{T}}=\frac{\partial(\nabla\mathbf{n})^{\mathrm{T}}}{\partial t}+(v\cdot\nabla)(\nabla\mathbf{n})^{\mathrm{T}}. \quad (25)$$

The contribution of $\mathbf{D}$ to $\dot{F}_{\mathrm{d}}$ appears to be different in the three nematic textures, which allows for identifying the contributions to elastic storage due to bulk orientation distortions. In this paper, we investigate the effect of anisotropic elasticity through the Frank distortion energy on the capillary instability of the LC fibres displaying the axial, onion and radial textures. The LC fibres are assumed inviscid so that the viscous dissipation term in equation (23) drops out and the transient integral energy balance equation becomes

$$\int_V\left[\frac{\partial}{\partial t}\left(\frac{1}{2}\rho v\cdot v\right)+\dot{F}_{\mathrm{d}}\right]\mathrm{d}V=\int_A\mathbf{N}\cdot\mathbf{t}\cdot v\,\mathrm{d}A. \quad (26)$$

The role of viscosity on the capillary instability of LC fibres has been studied with the governing nemato-capillary equations [25].

3. Results and discussion

The characterization of linear capillary instabilities in nematic fibres is based on the observation that two mechanisms are associated with the coupling between director, and hence the Frank distortion (gradient) elasticity, and the geometrical changes in the fibre: (i) surface tilting and (ii) surface displacement mechanisms. These two mechanisms are embedded in total distortion energy equations for statics:

$$\mathcal{F}_{\mathrm{d}}=\int_V F_{\mathrm{d}}\,\mathrm{d}V \quad (27)$$

and for dynamics:

$$\frac{\mathrm{d}\mathcal{F}_{\mathrm{d}}}{\mathrm{d}t}=\int_{V(t)}\dot{F}_{\mathrm{d}}\,\mathrm{d}V \quad (28)$$

and are activated for specific textures, as follows.

(i) Surface tilting mechanism ($\mathrm{M_T}$). The surface tilting mechanism is activated when surface tilting changes the director orientation. When splay and/or bend distortions arise due to the surface tilting driven by the re-orientation of the fibre surface, they tend to stabilize the fibres by increasing the Frank distortion energy. Hence, the $\mathrm{M_T}$ mechanism always promotes stability.

(ii) Surface displacement mechanism ($\mathrm{M_D}$). The surface displacement mechanism is characterized by decreasing the Frank distortion energy and thus destabilizing the nematic fibres. When splay and/or bend distortions are uncoupled from the surface orientation, the surface displacement may destabilize the fibres by decreasing the Frank distortion energy.

In what follows we discuss these two different instability mechanisms in axial, onion and radial fibres for statics and dynamics, and determine the parametric dependence of the nematic capillary instabilities on each mechanism of the Frank distortion elasticity.

3.1. *Static energy analysis*

In this section we present the thermodynamic analysis of the nematic fibre capillary instability for the axial, onion, and radial textures and establish the parametric conditions that lead to the Rayleigh instability.

Using Eqs. (1), (2) and (3), the surface free energy of the deformed LC fibre, $\mathcal{F}_{s,f}$, is obtained by integrating the second term in equation (16) over the surface with a unit wavelength, $\lambda=2\pi/k$, to order ξ_0^2:

$$\mathcal{F}_{s,f}=\gamma 2\pi\int_0^{\lambda}R(z)\left[1+\left(\frac{\mathrm{d}R}{\mathrm{d}z}\right)^2\right]^{\frac{1}{2}}\mathrm{d}z = \gamma 2\pi a\lambda-\gamma 2\pi a\lambda\frac{\xi_0^2}{4a^2}\left(1-\frac{4\pi^2a^2}{\lambda^2}\right). \quad (29)$$

Hence, the surface free energy change, Δ_s, is given as

$$\Delta_s\equiv\mathcal{F}_{s,f}-\mathcal{F}_{s,i}=-\gamma 2\pi a\lambda\frac{\xi_0^2}{4a^2}\left(1-\frac{4\pi^2a^2}{\lambda^2}\right) = -\gamma\pi^2\xi_0^2\frac{1}{ka}\left(1-k^2a^2\right) \quad (30)$$

where $\mathcal{F}_{s,i}$ is the initial surface free energy of the

cylindrical fibre:

$$\mathcal{F}_{s,i} = \gamma 2\pi a\lambda. \tag{31}$$

3.1.1. *Axial fibres*

The distorted director field for each texture is obtained by solving equation (14) with (15). Using equations (9) and (12), the distorted director field of the initially axial texture can be written as

$$\mathbf{n}^{\mathrm{A}}(r, z) = \mathbf{i}_z + n_r(r, z)\mathbf{i}_r \tag{32}$$

where n_r is the slight splay–bend director distortion as a function of r and z. Substituting equations (32) and (15) into (14) results in

$$\left(\nabla^2\mathbf{n}\right)_r = \frac{\partial^2 n_r}{\partial r^2} + \frac{1}{r}\frac{\partial n_r}{\partial r} + \frac{\partial^2 n_r}{\partial z^2} - \frac{n_r}{r^2} = 0 \tag{33}$$

where $(\nabla^2\mathbf{n})_r$ is the r-component of the vector $\nabla^2\mathbf{n}$. By solving equation (33) and using periodic and finite boundary conditions in the z- and r-directions, respectively, the splay–bend distortion is found to be

$$n_r(r, z) = -\xi_0 k \sin[kz]\frac{I_1[kr]}{I_1[ka]} \tag{34}$$

where $I_1[x]$ is the modified Bessel function of the first kind of order 1. In deriving equation (34), the strong anchoring condition that the director field is parallel to the planar easy axis (perpendicular to the unit surface normal) at the surface is applied. Thus, the distorted director field for the axial texture is

$$\mathbf{n}^{\mathrm{A}}(r, z) = \mathbf{i}_z - \xi_0 k \sin[kz]\frac{I_1[kr]}{I_1[ka]}\mathbf{i}_r. \tag{35}$$

The elastic energy for the axial fibre is initially zero because no director gradients initially exist, and only arises with the distorted director field due to surface tilting. Using equation (35), the elastic distortion free energy, $\mathcal{F}_{d,f}$, in equation (27) is obtained by integrating the first term in equations (16), over the volume with a unit wavelength, $\lambda = \frac{2\pi}{k}$, to order ξ_0^2:

$$\begin{aligned}\mathcal{F}_{d,f} &= 2\pi\int_0^{\frac{2\pi}{k}}\int_0^{R(z)}\frac{K}{2}\left[(\nabla\cdot\mathbf{n})^2 + (\nabla\times\mathbf{n})^2\right] r\,\mathrm{d}r\,\mathrm{d}z \\ &= \pi^2\xi_0^2\frac{K}{a}k^2a^2\frac{I_0[ka]}{I_1[ka]}\end{aligned} \tag{36}$$

where $I_0[x]$ is the modified Bessel function of the first kind of order 0. The distortion free energy change, Δ_{d}, is given as

$$\Delta_d \equiv \mathcal{F}_{d,f} - \mathcal{F}_{d,i} = \pi^2\xi_0^2\frac{K}{a}k^2a^2\frac{I_0[ka]}{I_1[ka]}. \tag{37}$$

From equations (30) and (37), the net change in the total free energy, Δ, for the axial fibre is given by

$$\Delta = \Delta_s + \Delta_d = \pi^2\xi_0^2\frac{\gamma}{ka}\left[\left(k^2a^2 - 1\right) + \frac{K}{a\gamma}k^3a^3\frac{I_0[ka]}{I_1[ka]}\right]. \tag{38}$$

By setting

$$\Delta = 0, \tag{39}$$

meaning that no total free energy change occurs, the dimensionless critical wavenumber $(ka)_{\mathrm{c}}$ and the critical wavelength λ_c are found as

$$(ka)_c = \frac{2\pi a}{\lambda_c} = \frac{1}{\left(1 + 2\frac{K}{\gamma a}\right)^{\frac{1}{2}}}, \quad \lambda_c = \lambda_R\left(1 + 2\frac{K}{\gamma a}\right)^{\frac{1}{2}}, \tag{40}$$

$$\lambda_R = 2\pi a \tag{41}$$

where λ_{R} is the critical wavelength for isotropic liquid fibres, known as the Rayleigh capillary instability threshold. From equation (40), the net effect of Frank elasticity is to stabilize the fibre by splay–bend distortions in the rz-plane. In other words, the surface tilting mechanism, $\mathrm{M_T}$, acting through splay–bend modes due to $n_r(r, z)$ created on the rz-plane tends to stabilize the fibre by increasing the Frank distortion energy:

$$\mathrm{M_T} : \mathbf{n}_0^A = (0, 0, 1) \Rightarrow \mathbf{n}^A = (n_r(r, z), 0, 1). \tag{42}$$

3.1.2. *Onion fibres*

In the onion texture, axial (z-directional) periodic surface disturbances do not affect the azimuthal (θ-directional) director field because the fibre shape and the director field are uncoupled. Thus, the director field remains unchanged by changes in the geometry:

$$\mathbf{n}^O = \mathbf{n}_0^O = \mathbf{i}_\theta. \tag{43}$$

The Frank elasticity for the onion texture is pure bend and arises because the molecules bend azimuthally (see figure 2 (*b*)); then the initial elastic distortion energy $\mathcal{F}_{d,i}$ is obtained as

$$\mathcal{F}_{d,i} = 2\pi\int_0^{\frac{2\pi}{k}}\int_{r_0}^{a}\frac{K}{2}(\nabla\times\mathbf{n})^2 r\,\mathrm{d}r\,\mathrm{d}z = \pi K\frac{2\pi}{k}\ln\frac{a}{r_0} \tag{44}$$

where r_0 is the defect core radius [22]. Because of the existence of the defect core at the centre of the onion fibre, the lower integration limit in the r-direction is r_0. It is known that the defect core radius r_0 is in the order of nanometers [22]. Although the director field remains unchanged during the fibre deformation, the elastic distortion energy $\mathcal{F}_{d,f}$ changes due to the fibre

displacements and is obtained to order ξ_0^2:

$$\begin{aligned}\mathcal{F}_{d,f} &= 2\pi \int_0^{\frac{2\pi}{k}} \int_{r_0}^{R(z)} \frac{K}{2} (\nabla \times \mathbf{n})^2 r \, \mathrm{d}r \, \mathrm{d}z \\ &= \pi K \frac{2\pi}{k} \left(\ln \frac{a}{r_0} - \frac{\xi_0^2}{2a^2} \right) .\end{aligned} \tag{45}$$

The distortion free energy change Δ_d is given as

$$\Delta_d = -\pi^2 \xi_0^2 \frac{K}{a} \frac{1}{ka}. \tag{46}$$

From equations (30) and (46), the net change in the total free energy Δ for the onion fibre is given by

$$\Delta = \pi^2 \xi_0^2 \frac{\gamma}{ka} \left[(k^2 a^2 - 1) - \frac{K}{a\gamma} \right]. \tag{47}$$

Using equation (39), the dimensionless critical wavenumber and the critical wavelength are found as

$$(ka)_c = \frac{2\pi a}{\lambda_c} = \left(1 + \frac{K}{\gamma a} \right)^{\frac{1}{2}}, \quad \lambda_c = \frac{\lambda_R}{\left(1 + \frac{K}{\gamma a} \right)^{\frac{1}{2}}}. \tag{48}$$

From equation (48), it is found that the net effect of Frank elasticity is to destabilize the fibre by reducing azimuthal bend energy. In other words, the surface displacement mechanism, $\mathrm{M_D}$, acting on the azimuthal bend modes tends to destabilize the fibre by decreasing the Frank distortion energy:

$$\begin{aligned}&\mathrm{M_D} \text{ for } \mathbf{n}^O = (0, 1, 0) = \text{constant} : \\ &\int_V F_d(\mathbf{n}^O) \, \mathrm{d}V \Rightarrow \int_{V^*} F_d(\mathbf{n}^O) \, \mathrm{d}V^*\end{aligned} \tag{49}$$

where V^* is the fibre volume with surface disturbances.

3.1.3. *Radial fibres*

Using equations (11) and (12), the distorted director field of the initially radial texture can be written as

$$\mathbf{n}^R(r, z) = \mathbf{i}_r + n_z(r, z) \mathbf{i}_z \tag{50}$$

where n_z is the slight bend distortion as a function of r and z. Substituting equations (50) and (15) into (14) results in

$$(\nabla^2 \mathbf{n})_z - n_z (\nabla^2 \mathbf{n})_r = \frac{\partial^2 n_z}{\partial r^2} + \frac{1}{r} \frac{\partial n_z}{\partial r} + \frac{\partial^2 n_z}{\partial z^2} + \frac{n_z}{r^2} = 0 \tag{51}$$

where $(\nabla^2 \mathbf{n})_z$ is the z-component of the vector $\nabla^2 \mathbf{n}$. Since the second partial derivative of n_z with respect to z in equation (51) is much smaller than the other terms when estimating the order of magnitude, adopting the long wavelength approximation, i.e.

$$\frac{\lambda}{a} \gg 1 \tag{52}$$

enables us to solve a quasi-one-dimensional ordinary differential equation:

$$\frac{\partial^2 n_z}{\partial r^2} + \frac{1}{r} \frac{\partial n_z}{\partial r} + \frac{n_z}{r^2} = 0. \tag{53}$$

By using boundary conditions that the director field is perpendicular to the fibre axis at the defect core and periodic and parallel to the unit normal at the surface, the bend distortion is found to be

$$n_z(r, z) = \xi_0 k \sin[kz] \frac{\sin\left(\ln \frac{r}{r_0} \right)}{\sin\left(\ln \frac{a}{r_0} \right)}. \tag{54}$$

Thus, the distorted director field for the radial texture is

$$\mathbf{n}^R(r, z) = \mathbf{i}_r + \xi_0 k \sin[kz] \frac{\sin\left(\ln \frac{r}{r_0} \right)}{\sin\left(\ln \frac{a}{r_0} \right)} \mathbf{i}_z. \tag{55}$$

Therefore, in the long wavelength approximation, bend distortions on the rz-plane are taken into account. The Frank elasticity for the initially radial texture is pure splay and arises because the molecules splay radially, see figure 2 (*c*); then the initial elastic distortion energy $\mathcal{F}_{d,i}$ is obtained as

$$\mathcal{F}_{d,i} = 2\pi \int_0^{\frac{2\pi}{k}} \int_{r_0}^{a} \frac{K}{2} (\nabla \cdot \mathbf{n})^2 r \, \mathrm{d}r \, \mathrm{d}z = \pi K \frac{2\pi}{k} \ln \left(\frac{a}{r_0} \right). \tag{56}$$

It is also noted that the lower integration limit in the r-direction is r_0 because of the existence of the defect core at the centre of the radial fibre. Using equation (55), the elastic distortion free energy $\mathcal{F}_{d,f}$ is obtained for the deformed fibre to order ξ_0^2:

$$\begin{aligned}\mathcal{F}_{d,f} &= 2\pi \int_0^{\frac{2\pi}{k}} \int_{r_0}^{R(z)} \frac{K}{2} \left[(\nabla \cdot \mathbf{n})^2 + (\nabla \times \mathbf{n})^2 \right] r \, \mathrm{d}r \, \mathrm{d}z \\ &= \pi K \frac{2\pi}{k} \left\{ \ln \frac{a}{r_0} - \frac{\xi_0^2}{2a^2} + \frac{1}{4} \xi_0^2 k^2 \left[\frac{\ln \frac{a}{r_0}}{\sin^2\left(\ln \frac{a}{r_0} \right)} + \frac{\cos\left(\ln \frac{a}{r_0} \right)}{\sin\left(\ln \frac{a}{r_0} \right)} \right] \right\}.\end{aligned} \tag{57}$$

The distortion free energy change Δ_d is given as

$$\Delta_\mathrm{d} = \pi^2 \xi_0^2 \frac{K}{a} \frac{1}{ka} \left\{ -1 + \frac{1}{2} k^2 a^2 \left[\frac{\ln \frac{a}{r_0}}{\sin^2\left(\ln \frac{a}{r_0} \right)} + \frac{\cos\left(\ln \frac{a}{r_0} \right)}{\sin\left(\ln \frac{a}{r_0} \right)} \right] \right\}. \tag{58}$$

From equations (30) and (58), the net change in the total free energy Δ for the radial fibre is given by

$$\Delta = \pi^2 \xi_0^2 \frac{\gamma}{ka} \left[(k^2 a^2 - 1) - \frac{K}{a\gamma} \left\{ 1 - \frac{1}{2} k^2 a^2 \left[\frac{\ln \frac{a}{r_0}}{\sin^2\left(\ln \frac{a}{r_0} \right)} + \frac{\cos\left(\ln \frac{a}{r_0} \right)}{\sin\left(\ln \frac{a}{r_0} \right)} \right] \right\} \right]. \tag{59}$$

Using equation (39), the dimensionless critical wave

number and the critical wavelength are found as

$$(ka)_c = \frac{2\pi a}{\lambda_c} = \left(\frac{1+S}{1+B}\right)^{\frac{1}{2}}, \quad \lambda_c = \lambda_R \left(\frac{1+B}{1+S}\right)^{\frac{1}{2}} \tag{60}$$

$$S = \frac{K}{a\gamma}, \quad B = \frac{1}{2}\frac{K}{a\gamma}\left[\frac{\ln\frac{a}{r_0}}{\sin^2\left(\ln\frac{a}{r_0}\right)} + \frac{\cos\left(\ln\frac{a}{r_0}\right)}{\sin\left(\ln\frac{a}{r_0}\right)}\right]. \tag{61}$$

From equation (60), the radial texture contains two competing elastic modes: the destabilizing splay Frank elasticity mode, S, causing a decrease in the critical wavelength and the stabilizing bend Frank elasticity mode, B, causing an increase in the critical wavelength.

Using equation (13), the splay elastic energy scales with $1/r^2$ and the surface displacement plays a role to redistribute the nematic LC away from the high energy core while the bend elasticity arises due to the director variation along the fibre axis driven by surface shape undulation, and thus increases the Frank elastic energy by director distortions. In other words, the surface displacement mechanism, M_D, acting on the splay modes on the $r\theta$-plane, tends to destabilize the fibre by decreasing the Frank distortion energy:

$$M_D \text{ for } \mathbf{n}^R = (1, 0, 0) = \text{constant}: \quad \int_V F_d(\mathbf{n}^R)\,dV \Rightarrow \int_{V^*} F_d(\mathbf{n}^R)\,dV^* \tag{62}$$

while the surface tilting mechanism, M_T, acting through bend modes due to $n_z(r, z)$ created on the rz-plane tends to stabilize the fibre by increasing the Frank distortion energy:

$$M_T : \mathbf{n}_0^R = (1, 0, 0) \Rightarrow \mathbf{n}^R = (1, 0, n_z(r, z)). \tag{63}$$

For micrometer-size fibres, we assume that $a = 10^{-5}$ m and $r_0 = 10^{-9}$ m [22]. Using these values, the splay mode S is approximately one hundred times smaller than the bend mode B so that the net effect of Frank elasticity on the capillary instability is to increase the critical wavelength above the Rayleigh threshold.

Figure 3 shows the scaled critical wavelength λ_c/λ_R as a function of the dimensionless energy ratio $K/a\gamma$; the dimensionless number $K/a\gamma$ is the ratio of the bulk elastic energy to the isotropic surface energy, for the three nematic textures. In both plots, the reference horizontal line corresponds to the Rayleigh instability threshold for isotropic materials. Figure 3 (*a*) shows the global features of the effect of texture on the instability. The axial and radial textures tend to stabilize the fibre while the onion texture tends to destabilize the fibre. Thus, the effect of the energy ratio $K/a\gamma$ on the instability is texture dependent. The strongest effect is for the axial texture, where no saturation is observed. This is because the stabilizing surface tilting mechanism, M_T, increases monotonically. On the other hand, for the radial texture, as the energy ratio increases above a value of approximately ten, the stabilizing surface tilting mechanism, M_T, and destabilizing surface displacement mechanism, M_D, described above cancel each other, and the dimensionless critical threshold saturates at a value of 9.97. The threshold of the onion texture decreases to zero, since only the purely destabilizing surface displacement mechanism, M_D, is present. For nematic liquid crystals and micrometer-size fibres, it is expected that $K/a\gamma \leq 1$. For typical low molecular mass nematic LC fibres at temperatures sufficiently far from the smectic A transition (if any), using $\gamma = 10^{-2}\,\mathrm{N\,m^{-1}}$ [7], $K = 10^{-11}\,\mathrm{J\,m^{-1}}$ [34] and $a = 10^{-5}$ m, we find $\frac{K}{a\gamma} = 10^{-4}$. Meanwhile, nematic liquid crystalline polymers can have elastic constants of orders of magnitude up to $10^{-8}\,\mathrm{J\,m^{-1}}$ [35]. For mesophase carbon pitches, elastic constants were estimated to be of the

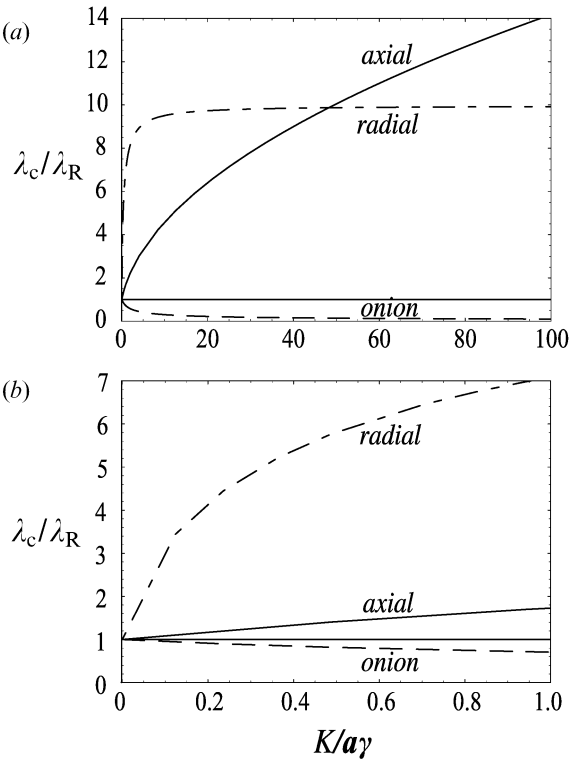

Figure 3. (*a*) Scaled critical wavelength λ_c/λ_R as a function of the dimensionless energy ratio $K/a\gamma$; the dimensionless number $K/a\gamma$ is the ratio of the bulk elastic energy to the isotropic surface energy, for the three nematic textures. In both plots, the reference horizontal line corresponds to the Rayleigh instability threshold for isotropic materials. The symbol λ_R is the critical Rayleigh wavelength given in equation (41). The figure shows that Frank elasticity stabilizes the axial and radial fibres, but destabilizes the onion texture. (*b*) Same as (*a*) but $0 < \frac{K}{a\gamma} < 1$. The figure shows that for this parametric window, Frank elasticity has the strongest impact on stability of the radial texture.

order of $10^{-8}\,\mathrm{J\,m^{-1}}$ [36]. In addition, near the nematic/smectic A transition, the bend elastic constant diverges [22, 37]. Therefore, with $K=10^{-8}\,\mathrm{J\,m^{-1}}$, the dimensionless parameter $\frac{K}{a\gamma}$ approaches one for micrometer-radius fibres, and hence figure 3 (*b*) focuses on the small $K/a\gamma$ regime. This figure shows that in this parametric window the strongest effect of Frank elasticity is on the stabilization of the radial texture.

3.2. *Transient energy analysis*

Figure 4 summarizes the complete phenomenology of the two Frank elasticity instability mechanisms in the transient energy analysis. The stabilizing surface tilting mechanism, $\mathrm{M_T}$, contributes to the distortion energy through the local time derivative and acts in the axial fibre by splay–bend modes and in the radial fibre by bend modes, created on the *rz*-plane. The destabilizing surface displacement mechanism, $\mathrm{M_D}$, contributes to the distortion energy through the convective change and acts in the onion fibre (uniform azimuthal bend modes) and in the radial fibre (uniform radial splay modes), in the $r\theta$-plane.

We next present the transient integral energy balance equation for the nematic fibre, derive the instability criteria for the three representative nematic textures (see figure 2), and discuss in detail the physical and mathematical aspects of the process.

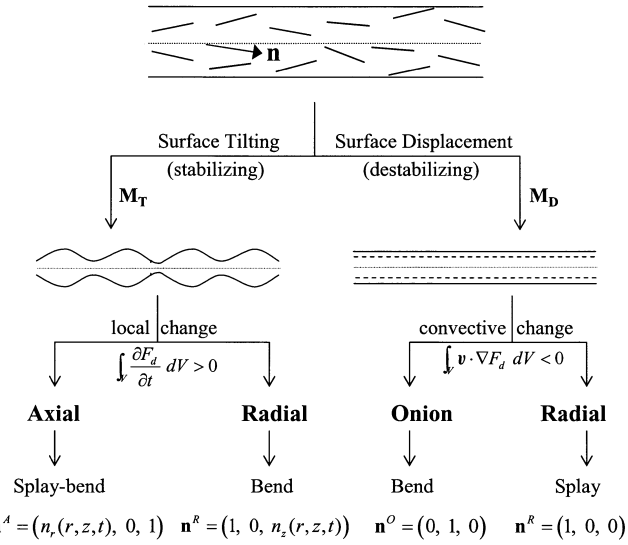

Figure 4. Frank elasticity instability mechanisms in the transient energy analysis. The stabilizing surface tilting mechanism $\mathrm{M_T}$ arises through the local time derivative and acts in the axial fibre by splay–bend modes and in the radial fibre by bend modes. The destabilizing surface displacement mechanism $\mathrm{M_D}$ arises through the convective change and acts in the onion fibre (uniform azimuthal bend modes) and in the radial fibre (uniform radial splay modes).

For the inviscid liquid fibre, the velocity field can be obtained by introducing the velocity potential and solving Laplace's equation of the velocity potential, which satisfies the continuity equation [2, 38, 39]:

$$\begin{aligned} \upsilon_r(r,\,z,\,t) &= \xi_0\alpha\exp(\alpha t)\cos[kz]\frac{I_1[kr]}{I_1[ka]},\\ \upsilon_z(r,\,z,\,t) &= -\xi_0\alpha\exp(\alpha t)\sin[kz]\frac{I_0[kr]}{I_1[ka]}. \end{aligned} \tag{64}$$

Using this velocity field in equation (64), the rate of change of kinetic energy in (26) is calculated in a unit wavelength $\lambda=\frac{2\pi}{k}$ to order ξ_0^2 as

$$\int_V \frac{\partial}{\partial t}\left(\frac{1}{2}\rho\upsilon\cdot\upsilon\right)\mathrm{d}V = \xi_0^2\alpha^3\exp(2\alpha t)\frac{2\pi^2\rho a}{k^2}\frac{I_0[ka]}{I_1[ka]}. \tag{65}$$

By assuming no surface shear, the surface integral term in equation (26) is rewritten as [25]

$$\int_A \mathbf{N}\cdot\mathbf{t}\cdot\upsilon\,\mathrm{d}A = \int_A (\nabla_\mathrm{s}\cdot\mathbf{t}^{se})\cdot\upsilon\,\mathrm{d}A = \int_A -p_\gamma\upsilon_r\,\mathrm{d}A \tag{66}$$

where $\mathbf{t}^{\mathrm{se}}$ is the surface elastic stress tensor and p_γ is the capillary pressure that is the magnitude of the surface normal force and is given using equations (8) and (17):

$$-p_\gamma = 2H\gamma = -\frac{\gamma}{a}+\frac{\gamma}{a^2}\left(1-k^2a^2\right)\xi_0\exp(\alpha t)\cos[kz]. \tag{67}$$

By substituting equations (64) and (67) into (66), the surface integral term is obtained in a unit wavelength $\lambda=2\pi/k$ to order ξ_0^2 as

$$\int_A \mathbf{N}\cdot\mathbf{t}\cdot\upsilon\,\mathrm{d}A = \xi_0^2\alpha\exp(2\alpha t)\frac{2\pi^2\gamma}{ka}\left(1-k^2a^2\right). \tag{68}$$

3.2.1. *Capillary instabilities in axial fibres*

Referring to equation (35), the distorted director field in the transient analysis can be written by assuming an exponential change in time:

$$\mathbf{n}^A(r,\,z,\,t) = \mathbf{i}_z - \xi_0 k\exp(\alpha t)\sin[kz]\frac{I_1[kr]}{I_1[ka]}\mathbf{i}_r. \tag{69}$$

It is noted that the flow driven by the capillary instability is so weak that the director field is unaffected by the flow [22].

As expected from the previous section, the rate of change of Frank distortion energy, $\dot{F}_\mathrm{d}$, is different in the three nematic textures. For the distorted axial texture in equation (69), the convective term in (25) is of higher order and disappears in the linear regime of the capillary instability while the local time derivative term contributes to $\dot{F}_\mathrm{d}$, which by using equation (24) is given by:

$$\dot{F}_d = K\left[\alpha\left(\frac{-\xi_0 k}{I_1[ka]}\exp(\alpha t)\right)^2\left\{(\sin[kz]kI_0[kr])^2+(\cos[kz]kI_1[kr])^2\right\}\right]. \tag{70}$$

Thus, using equation (70), equation (28) is obtained in a unit wavelength $\lambda = \frac{2\pi}{k}$ to order ξ_0^2:

$$\int_V \dot{F}_d \, dV = 2\pi^2 K \xi_0^2 k\alpha \exp(2\alpha t) ka \frac{I_0[ka]}{I_1[ka]}. \tag{71}$$

Substituting equations (65), (68) and (71) into (26) gives a quadratic equation for the dimensionless growth rate, $\alpha^* = \alpha\left(\rho a^3/\gamma\right)^{\frac{1}{2}}$:

$$\alpha^{*2} - \frac{(ka)^2}{2}\left[1 - \left(2\frac{K}{a\gamma} + 1\right)(ka)^2\right] = 0 \tag{72}$$

where ka is the dimensionless wave number. Solving the quadratic equation for α^*, equation (72), we find

$$\alpha^* = (ka)\left[\frac{1 - \left(2\frac{K}{a\gamma} + 1\right)(ka)^2}{2}\right]^{\frac{1}{2}}. \tag{73}$$

Thus, the axial fibres are unstable when the following inequality is satisfied:

$$1 - \left(2\frac{K}{a\gamma} + 1\right)(ka)^2 > 0. \tag{74}$$

The maximum growth rate $\alpha^*_{\max}$ and the corresponding wavenumber $ka_{\max}$ are obtained by solving equation (72):

$$ka_{\max} = \left[\frac{1}{2\left(2\frac{K}{a\gamma} + 1\right)}\right]^{\frac{1}{2}}, \quad \alpha^*_{\max} = \frac{1}{2}\left[\frac{1}{2\left(2\frac{K}{a\gamma} + 1\right)}\right]^{\frac{1}{2}} \tag{75}$$

which predict the axial fibre breakup into droplets with a characteristic size of $2\pi/ka_{\max}$ [40]. Equation (75) properly reduces to the well known results [38] when the bulk elastic anisotropy vanishes, i.e. $K = 0$, and the asymptotic results for the inviscid fibre are

$$\alpha^*_{\max} = \frac{1}{2\sqrt{2}}, \quad ka_{\max} = \frac{1}{\sqrt{2}}. \tag{76}$$

Solving equation (73) by setting $\alpha^* = 0$ gives the cut-off wave number:

$$ka_{\text{cutoff}} = \frac{1}{\left(1 + 2\frac{K}{\gamma a}\right)^{\frac{1}{2}}} \tag{77}$$

which is consistent with the critical wavenumber in the static energy analysis, equation (40).

Figure 5 shows the dimensionless growth rate curves α^* as a function of dimensionless wavenumber ka at $K/a\gamma = 0.1$, 1, 5 for the axial fibre. Not only ka_{cutoff} but $\alpha^*_{\max}$ and $ka_{\max}$ decrease as $K/a\gamma$ increases, meaning that the bulk elasticity suppresses the axial fibre instability by increasing the length scale of the capillary instability as well as slowing down its growth rate.

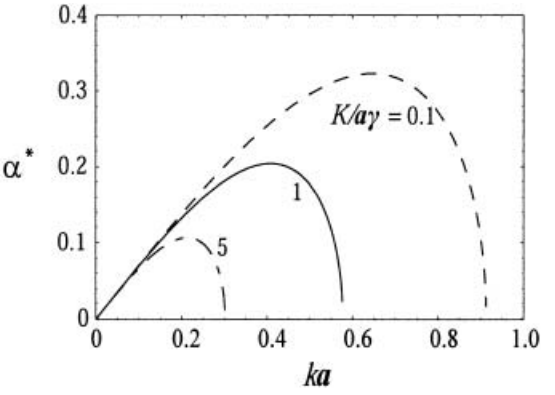

Figure 5. Dimensionless growth rate curves α^* as a function of dimensionless wavenumber ka for $K/a\gamma = 0.1$, 1, 5 for the axial fibre. Frank elasticity decreases the growth rate and increases the wavelength of the fastest growing mode.

Consistent with the static energy analysis, the effect of Frank distortion energy change $\dot{F}_d$ on the capillary instability for the transient energy analysis is now explained in detail (see figure 4). From equation (71), it is seen that the net effect of Frank elasticity is to stabilize the fibre by increasing splay–bend elastic energy. The distorted axial texture contributes to $\dot{F}_d$ only through the local time derivative term in equation (25). The stabilization mechanism M_T, through splay–bend distortions in the rz-plane is generated by changes in the surface orientation, and hence no contribution arises from the convective term which is related to changes in surface displacement.

3.2.2. *Capillary instabilities in onion fibers*

For the onion texture, the director field remains constant and the local time derivative term in equation (25) is zero while the convective term contributes to the Frank distortion energy change $\dot{F}_d$. In order to simplify the calculation of $\dot{F}_d$, we adopt standard approximations for the velocity field used previously in the literature [39]. From equation (64), it is evident that v_z is only weakly dependent on r and is assumed to be only a function of z while v_r is approximated linearly dependent on r. These approximations are considerably accurate when $ka < 1$. Then, the velocity field for the inviscid liquid is given as [39]

$$\begin{aligned} v_r(r, z, t) &= \xi_0 \alpha \exp(\alpha t)\frac{r}{a}\cos[kz], \\ v_z(z, t) &= -\xi_0 \alpha \exp(\alpha t)\frac{2}{ka}\sin[kz] \end{aligned} \tag{78}$$

which satisfies the continuity equation. Using equations (24)

and (78), it is found that

$$\dot{\boldsymbol{F}}_d = -K\frac{\xi_0\alpha\exp(\alpha t)}{a}\frac{\cos[kz]}{r^2}. \tag{79}$$

Thus, using equation (79), equation (28) is obtained in a unit wavelength $\lambda = 2\pi/k$ to order ξ_0^2 by

$$\int_V \dot{\boldsymbol{F}}_d \, \mathrm{d}V = -2\pi^2\xi_0^2\alpha\exp(2\alpha t)\frac{K}{a}\frac{1}{ka}. \tag{80}$$

Substituting equations (65), (68) and (80) into (26) gives a quadratic equation for the dimensionless growth rate:

$$\alpha^{*2} - \frac{(ka)^2}{2}\left[1 + \frac{K}{a\gamma} - (ka)^2\right] = 0. \tag{81}$$

Solving the quadratic equation for α^*, equation (81), we find

$$\alpha^* = (ka)\left[\frac{1 + \dfrac{K}{a\gamma} - (ka)^2}{2}\right]^{\frac{1}{2}}. \tag{82}$$

Thus, the onion fibres are unstable when the following inequality is satisfied:

$$1 + \frac{K}{a\gamma} - (ka)^2 > 0. \tag{83}$$

The maximum growth rate $\alpha^*_{\max}$ and the corresponding wavenumber $ka_{\max}$ are obtained by solving equation (81):

$$ka_{\max} = \left(\frac{1 + \dfrac{K}{a\gamma}}{2}\right)^{\frac{1}{2}}, \quad \alpha^*_{\max} = \frac{1 + \dfrac{K}{a\gamma}}{2\sqrt{2}} \tag{84}$$

which predict the onion fibre break-up into droplets with a characteristic size of $2\pi/ka_{\max}$ [40]. Equation (84) properly reduces to the well known results, equation (76), when the bulk elastic anisotropy dependence vanishes, i.e. $K = 0$. Solving equation (82) by setting $\alpha^* = 0$ gives the cut-off wave number:

$$ka_{\text{cutoff}} = \left(1 + \frac{K}{\gamma a}\right)^{\frac{1}{2}} \tag{85}$$

which is consistent with the critical wave number in the static energy analysis, equation (48).

Figure 6 shows the dimensionless growth rate curves α^* as a function of dimensionless wavenumber ka at $K/a\gamma = 0.1$, 1, 5 for the onion fibre. Not only ka_{cutoff} but $\alpha^*_{\max}$ and $ka_{\max}$ increase as $K/a\gamma$ increases, meaning that the bulk elasticity promotes the onion fibre instability by decreasing the length scale of the capillary instability as well as increasing its growth rate. From equation (80), it is seen that the net effect of Frank elasticity is to destabilize the fibre by decreasing the azimuthal

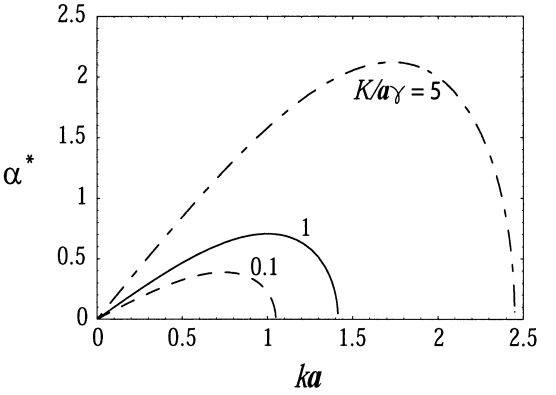

Figure 6. Dimensionless growth rate curves α^* as a function of dimensionless wavenumber ka at $K/a\gamma = 0.1$, 1, 5 for the onion fibre. Frank elasticity increases the growth rate and decreases the wavelength of the fastest growing mode.

bend Frank elastic energy. The surface displacement that leads to a decrease in the azimuthal bend energy contributes to $\dot{F}_{\mathrm{d}}$ only through the convective term in equation (25). Under the destabilization mechanism, $\mathrm{M_D}$, the destabilizing azimuthal bend modes arise from changes in the location of the surface, and hence no contribution from local time derivatives appears. The local time derivative contribution is, as noted above (see figure 4), only ignited by couplings between surface orientation and the director field. Since the director is uncoupled from surface orientation, only positional effects promote the instability.

3.2.3. *Capillary instabilities in radial fibres*

Referring to equation (55), the distorted director field in the transient analysis can be written by assuming an exponential change in time:

$$\mathbf{n}^R(r, z, t) = \mathbf{i}_r + \xi_0 k\exp(\alpha t)\sin[kz]\frac{\sin\left(\ln\dfrac{r}{r_0}\right)}{\sin\left(\ln\dfrac{a}{r_0}\right)}\mathbf{i}_z. \tag{86}$$

It is also noted that the flow driven by the capillary instability is so weak that the director field is not affected by the flow.

For the radial texture in equation (86), both the convective and the local time derivative terms in (25) remain and contribute to the Frank distortion energy change $\dot{F}_{\mathrm{d}}$, which is given using equations (24) and (78):

$$\dot{F}_{\mathrm{d}} = K\left[-\alpha\exp(\alpha t)\frac{\xi_0}{a}\cos[kz]\frac{1}{r^2} + \alpha\exp(2\alpha t)\frac{\xi_0^2k^2}{\sin^2\left(\ln\dfrac{a}{r_0}\right)}\sin^2[kz]\frac{\cos^2\left(\ln\dfrac{r}{r_0}\right)}{r^2}\right]. \tag{87}$$

Thus, using equation (87), equation (28) is obtained in a

unit wavelength $\lambda = 2\pi/k$ to order ξ_0^2 by

$$\int_V \dot{F}_d \, dV = -2\pi^2 \alpha \exp(2\alpha t) \xi_0^2 \frac{K}{a} \frac{1}{ka} \left\{ 1 - k^2 a^2 \frac{1}{2} \left[\frac{\ln\frac{a}{r_0}}{\sin^2\left(\ln\frac{a}{r_0}\right)} + \frac{\cos\left(\ln\frac{a}{r_0}\right)}{\sin\left(\ln\frac{a}{r_0}\right)} \right] \right\}. \quad (88)$$

Substituting equations (65), (68) and (88) into (26) gives a quadratic equation for the dimensionless growth rate:

$$\alpha^{*2} - \frac{(ka)^2}{2} \left[\left(1 + \frac{K}{a\gamma}\right) - (ka)^2 \left\{ 1 + \frac{1}{2}\frac{K}{a\gamma} \left[\frac{\ln\frac{a}{r_0}}{\sin^2\left(\ln\frac{a}{r_0}\right)} + \frac{\cos\left(\ln\frac{a}{r_0}\right)}{\sin\left(\ln\frac{a}{r_0}\right)} \right] \right\} \right] = 0. \quad (89)$$

Solving the quadratic equation for α^*, equation (89), we find

$$\alpha^* = \frac{ka}{\sqrt{2}} \left[\left(1 + \frac{K}{a\gamma}\right) - (ka)^2 \left\{ 1 + \frac{1}{2}\frac{K}{a\gamma} \left[\frac{\ln\frac{a}{r_0}}{\sin^2\left(\ln\frac{a}{r_0}\right)} + \frac{\cos\left(\ln\frac{a}{r_0}\right)}{\sin\left(\ln\frac{a}{r_0}\right)} \right] \right\} \right]^{\frac{1}{2}}. \quad (90)$$

Thus, the radial fibres are unstable when the following inequality is satisfied:

$$\left(1 + \frac{K}{a\gamma}\right) - (ka)^2 \left\{ 1 + \frac{1}{2}\frac{K}{a\gamma} \left[\frac{\ln\frac{a}{r_0}}{\sin^2\left(\ln\frac{a}{r_0}\right)} + \frac{\cos\left(\ln\frac{a}{r_0}\right)}{\sin\left(\ln\frac{a}{r_0}\right)} \right] \right\} > 0. \quad (91)$$

Meanwhile, equation (90) properly reduces to the well known result of Rayleigh when the bulk elastic anisotropy dependence vanishes, i.e. $K = 0$:

$$\alpha^* = \frac{ka}{\sqrt{2}} \left[1 - (ka)^2 \right]^{\frac{1}{2}} \quad (92)$$

and thus equation (76) is also obtained for $K = 0$. Solving equation (90) by setting $\alpha^* = 0$ gives the cut-off wave number:

$$ka_{\text{cutoff}} = \left\{ \frac{1 + \frac{K}{a\gamma}}{1 + \frac{1}{2}\frac{K}{a\gamma} \left[\frac{\ln\frac{a}{r_0}}{\sin^2\left(\ln\frac{a}{r_0}\right)} + \frac{\cos\left(\ln\frac{a}{r_0}\right)}{\sin\left(\ln\frac{a}{r_0}\right)} \right]} \right\}^{\frac{1}{2}} \quad (93)$$

which is consistent with the critical wave number in the static energy analysis, equation (60).

Figure 7 shows the dimensionless growth rate curves α^* as a function of dimensionless wave number ka, for $K/a\gamma = 0.323$, 1, 5 for the radial fibre. As $K/a\gamma$ increases, ka_{cutoff} and $ka_{\max}$ decrease while $\alpha^*_{\max}$ decreases until $K/a\gamma \sim 1$ and then increases, meaning that the bulk elasticity contains two competing effects on the radial fibre instability: (i) the suppressing effect shown by increasing the length scales of the capillary instability and (ii) the non-monotonic maximum growth rate. Surface tilting on the radial fibre ignites stabilizing bend modes on the rz-plane. These bending distortions under the M_T mechanism increase the energy and are thus stabilizing. On the other hand, the initial splay distortion is destabilizing under the M_D mechanism and promotes the instability. The stabilizing bend modes are driven by the orientation of the fibre surface (surface tilting), while the destabilizing splay modes act through changes in the position of the surface (surface displacement). The destabilizing splay modes in the radial textures are equivalent to the destabilizing azimuthal bend modes in the onion texture since they are controlled by the M_D mechanism (see figure 4). On the other hand, the stabilizing bend modes in the radial texture are equivalent to the stabilizing splay–bend modes in the axial texture since they are controlled by the M_T mechanism (see figure 4).

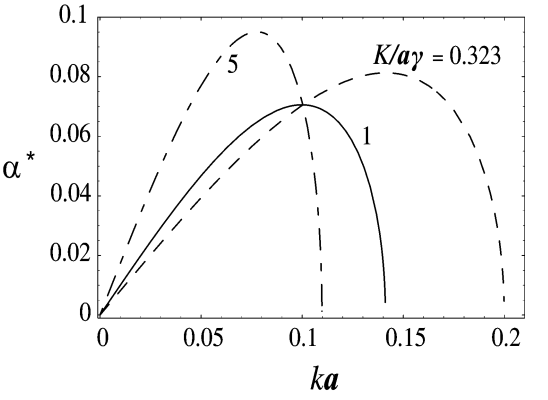

Figure 7. Dimensionless growth rate curves α^* as a function of dimensionless wavenumber ka at $K/a\gamma = 0.323$, 1, 5 for the radial fibre. Frank elasticity increases the wavelength of the fastest growing mode. On the other hand, the maximum growth rate is non-monotonic, first decreases and then increases with increasing $K/a\gamma$.

In partial summary, when splay and/or bend distortions are created by surface tilting they tend to stabilize the fibre by increasing the energy, and when splay and/or bend distortions are uncoupled from the surface orientation, the surface displacement may destabilize the fibres by decreasing the Frank distortion energy. In the transient integral energy analysis, surface tilting effects enter through local time derivatives while surface displacement effects enter through convective terms, see equation (25).

3.3. *Bulk elastic energy contributions to capillary instabilities*

This section briefly compares the Frank distortion energy contribution for each texture in the static energy

analysis to that in the transient energy analysis, with the objective of elucidating the dual nature of orientation gradients in growing peristaltic modes, as discussed in the previous section.

By making use of the divergence theorem and equations (24) and (25), equation (28) is rewritten as

$$\frac{\mathrm{d}\mathcal{F}_d}{\mathrm{d}t} = \int_V \frac{\partial F_d}{\partial(\nabla\mathbf{n})} : \frac{\partial\,(\nabla\mathbf{n})^{\mathrm{T}}}{\partial t}\,\mathrm{d}V + \int_S \mathbf{N}\cdot v F_d\,\mathrm{d}A. \quad (94)$$

In statics, the change of the distortion free energy corresponding to equation (94) can be expressed using the variational symbol δ:

$$\delta\mathcal{F}_d = \int_V \frac{\partial F_d}{\partial(\nabla\mathbf{n})} : \delta\,(\nabla\mathbf{n})^{\mathrm{T}}\,\mathrm{d}V + \int_S \mathbf{N}\cdot\delta\mathbf{s} F_d\,\mathrm{d}A \quad (95)$$

where $\delta\mathbf{s}$ is the variation of the position vector at the surface.

From equations (94) and (95), it is clearly seen that in the linear regime considered here, the first integral represents the surface tilting contribution to the Frank distortion energy in the presence of director distortions, while the second represents the surface displacement contribution. The difference between the static and the transient analyses comes from time dependence of the system. Without time dependence, the free energy change is obtained for the system before and after surface disturbances as shown in the statics results. In both statics and dynamics, the stabilizing $\mathrm{M_T}$ mechanism is included in the first integral while the destabilizing $\mathrm{M_D}$ mechanism is in the second integral. The correspondence between the statics and dynamics is shown by the consistency between results in equations (37), (46) and (58), and results in (71), (80) and (88). In all textures, the static thresholds, shown in equations (40), (48) and (60), are consistent with the corresponding cut-off results from the transient analysis, shown in (77), (85) and (93). This consistency establishes the correctness of the two distinct approaches.

4. Conclusions

Capillary instabilities in nematic fibres reflect the anisotropic nature of liquid crystals. Classical theories of liquid crystalline materials are used to develop static and transient thermodynamic models of linear axisymmetric capillary instabilities driven by surface area reduction. Since the bulk gradient elasticity of nematics contains orientation gradient contributions that couple with surface distortions, the thermodynamic models on three representative nematic fibre textures identify the most likely effects. The axial texture tends to stabilize the fibre by increasing splay–bend elastic energy created by the surface tilting mechanism. The onion texture tends to destabilize the fibre by decreasing azimuthal bend elastic energy created by the surface displacement mechanism. The peristaltic distortion in the radial texture creates two competing splay and bend elastic modes driven by surface displacement and surface tilting, respectively. By estimating the model parameters using published data for typical low molecular mass nematic LC fibres, it is found that the net effect of Frank elasticity is to increase the length scales of the capillary instability in the radial fibre. The use of static and dynamic formulations gives mutually consistent results, and shows that the role of Frank elasticity in capillary instabilities is a function of the initial fibre texture. Splay and/or bend modes on the rz-plane stabilize the fibre by the surface tilting mechanism while splay and/or bend modes on the $r\theta$-plane destabilize it by the surface displacement mechanism. Gradient elasticity offers another tool to control soft evolving surfaces.

References

[1] Edwards, D. A., Brenner, H., and Wasan, D. T., 1989, *Interfacial Transport Processes and Rheology* (Boston: Butterworths-Heinemann).

[2] Levich, V. G., 1962, *Physicochemical Hydrodynamics* (Englewood Cliffs: Prentice-Hall).

[3] Slattery, J. C., 1990, *Interfacial Transport Phenomena* (New York: Springer-Verlag).

[4] Edie, D. D., and Stoner, E. G., 1993, in *Carbon-Carbon Materials and Composites*, edited by J. D. Buckley and D. D. Edie (Park Ridge: Noyes).

[5] Rey, A. D., 1997, *Ind. Eng. Chem. Res.*, **36,** 1114.

[6] Blinov, L. M., and Chigrinov, V. G., 1994, *Electrooptic Effects in Liquid Crystal Materials* (New York: Springer-Verlag).

[7] Sonin, A. A., 1995, *The Surface Physics of Liquid Crystals* (Amsterdam: Gordon and Breach).

[8] Jerome, B., 1998, in *Handbook of Liquid Crystals*, Vol. 1, edited by D. Demus, J. Goodby, G. W. Gray, H.-W. Spiess and V. Vill (Weinheim: Wiley-VCH).

[9] Yokoyama, H., 1997, in *Handbook of Liquid Crystal Research*, edited by P. J. Collins and J. S. Patel (New York: Oxford University Press).

[10] Chandrasekhar, S., 1992, *Liquid Crystals* (Cambridge: Cambridge University Press).

[11] Sluckin, T. J., and Poniewierski, A., 1986, in *Fluid Interfacial Phenomena*, edited by C. A. Croxton (Chichester: John Wiley & Sons), pp. 215–253.

[12] Sen, A. K., and Sullivan, D. E., 1987, *Phys. Rev A.*, **35,** 1391.

[13] Faetti, S., 1991, in *Physics of Liquid Crystalline Materials*, edited by I.-C. Khoo and F. Simoni (Philadelphia: Gordon and Breach), pp. 301–336.

[14] Barbero, G., and Durand, G., 1996, in *Liquid Crystals in Complex Geometries*, edited by G. P. Crawford and S. Zumer (London: Taylor and Francis), pp. 21–52.

[15] Ericksen, J. L., 1976, in *Advances in Liquid Crystals*, Vol. 2, edited by G. H. Brown (New York: Academic Press), pp. 233–298.

[16] VIRGA, E. G., 1994, *Variational Theories for Liquid Crystals* (London: Chapman Hall).
[17] REY, A. D., 1999, *Liq. Cryst.*, **26,** 913.
[18] REY, A. D., 1999, *J. Chem. Phys.*, **110,** 9769.
[19] JENKINS, J. T., and BARRATT, P. J., 1974, *Quart. J. Mech. appl. Math.*, **27,** 111.
[20] PAPENFUSS, C., and MUSCHIK, W., 1992, *Mol. Mater.*, **2,** 1.
[21] POZRIKIDIS, C., 1997, *Introduction to Theoretical and Computational Fluid Dynamics* (New York: Oxford University Press).
[22] DE GENNES, P. G., and PROST, J., 1993, *The Physics of Liquid Crystals* (London: Oxford University Press).
[23] EHRENTRAUT, H., and HESS, S., 1995, *Phys. Rev. E*, **51,** 2202.
[24] LARSON, R. G., 1999, *The Structure and Rheology of Complex Fluids* (New York: Oxford University Press).
[25] CHEONG, A.-G., REY, A. D., and MATHER, P. T., 2001, *Phys. Rev. E*, **64,** 041701/1.
[26] CHEONG, A.-G., and REY, A. D., 2002, *J. Chem. Phys.*, **117,** 5062.
[27] CHEONG, A.-G., and REY, A. D., 2002, *Eur. Phys. J. E*, **9,** 171.
[28] REY, A. D., 1999, *Model. Simul. mater. Sci. Eng.*, **7,** 147.
[29] CLADIS, P. E., and KLEMAN, M., 1972, *J. Phys.*, **33,** 591.
[30] MEYER, R. B., 1973, *Philos. Mag.*, **27,** 405.
[31] WILLIAMS, C., PIERANSKI, P., and CLADIS, P. E., 1972, *Phys. Rev. Lett.*, **29,** 90.
[32] WILLIAMS, C. E., CLADIS, P. E., and KLEMAN, M., 1973, *Mol. Cryst. liq. Cryst.*, **21,** 355.
[33] CRAWFORD, G. P., VILFAN, M., and DOANE, J. W., 1991, *Phys. Rev. A*, **43,** 835.
[34] KREUZER, M., and EIDENSCHINK, R., 1996, in *Liquid Crystals in Complex Geometries*, edited by G. P. Crawford and S. Zumer (London: Taylor & Francis), pp. 307–324.
[35] DE'NEVE, T., KLEMAN, M., and NAVARD, P., 1994, *Liq. Cryst.*, **18,** 67.
[36] FLEUROT, O., and EDIE, D. D., 1998, *J. Rheol.*, **42,** 781.
[37] CHEUNG, L., and MEYER, R. B., 1973, *Phys. Lett. A*, **43,** 261.
[38] MIDDLEMAN, S., 1995, *Modeling Axisymmetric Flows: Dynamics of Films, Jets, and Drops* (San Diego: Academic Press).
[39] ANNO, J. N., 1977, *Mechanics of Liquid Jets* (Toronto: Lexington Books).
[40] REY, A. D., 1997, *J. Phys. II Fr.*, **7,** 1001.